

RESEARCH

Open Access



Stability evaluation of a grid-tied hybrid wind/PV farm joined with a hybrid energy-storage system

Li Wang^{1*} , Wang Jun-Yi Ke¹, Rui-Xuan Wu¹, Manoj Tripathy², Hazlie Mokhlis³, Kein Huat Chua⁴, Anton V. Prokhorov⁵, Thi Ha Nguyen⁶, Mohammed Mehdi Farid⁷, Alison Subiantoro⁸, Kang Li⁹, Benjamin Chong⁹, Sadegh Azizi⁹, Amir Abiri Jahromi⁹ and Dehong Xu¹⁰

Abstract

This paper presents the stability-evaluation outcomes of a multimachine power system (MMPS) connected with a large-scale hybrid wind farm (WF) and photovoltaic (PV) farm or hybrid wind/PV farm (HWPF) and a hybrid energy-storage system (HESS) consisting of a vanadium redox flow battery (VRFB) and a supercapacitor (SC). A probability scheme is used to determine the rated power of the proposed HESS, where the capacities of the VRFB-ESS and the SC-ESS are designed to effectively utilize their operating features. The control strategy of the HESS is proposed to reduce the pressure of the VRFB-ESS and smooth the output power fluctuations of the HWPF. The steady-state stability, small-signal stability, dynamic performances, and transient simulations of the studied grid-tied HWPF fed to the MMPS with and without the HESS are achieved. The simulation outcomes show that the proposed HESS can enhance the stability and power-smoothing performance of the HWPF fed to the MMPS.

Keywords Wind farm, PV farm, Hybrid wind/PV farm, Hybrid energy-storage system, Vanadium redox flow battery, Supercapacitor, Multimachine power system, Stability, Power smoothing

*Correspondence:

Li Wang
liwangncku@gmail.com

¹ Department of Electrical Engineering, National Cheng Kung University, Tainan 701401, Taiwan

² Department of Electrical Engineering, Indian Institute of Technology Roorkee, Roorkee, Uttarakhand 247667, India

³ Department of Electrical Engineering, Faculty of Engineering, University of Malaya, Kuala Lumpur 50603, Malaysia

⁴ Department of Electrical and Electronic Engineering, Faculty of Engineering and Science, Universiti Tunku Abdul Rahman, Kuala Lumpur 53300, Malaysia

⁵ Institute of Power Engineering, Tomsk Polytechnic University, Tomsk 634050, Russia

⁶ Eversource Energy Center, University of Connecticut, Storrs 06269, USA

⁷ Chemical and Materials Engineering, University of Auckland, Auckland 1010, New Zealand

⁸ Mechanical Engineering, University of Auckland, Auckland 1010, New Zealand

⁹ School of Electronic and Electrical Engineering and Smart Energy Systems, University of Leeds, Leeds LS2 9JT, UK

¹⁰ Power Electronics Institute, Zhejiang University, Hangzhou 310058, China



© The Author(s) 2023. **Open Access** This article is licensed under a Creative Commons Attribution 4.0 International License, which permits use, sharing, adaptation, distribution and reproduction in any medium or format, as long as you give appropriate credit to the original author(s) and the source, provide a link to the Creative Commons licence, and indicate if changes were made. The images or other third party material in this article are included in the article's Creative Commons licence, unless indicated otherwise in a credit line to the material. If material is not included in the article's Creative Commons licence and your intended use is not permitted by statutory regulation or exceeds the permitted use, you will need to obtain permission directly from the copyright holder. To view a copy of this licence, visit <http://creativecommons.org/licenses/by/4.0/>.

1 Introduction

The huge increase in energy demands and fast shortage of fossil fuels significantly demonstrate the importance of employing alternative power-production schemes. Renewable energy sources (RES) and especially wind/PV-based power-generation systems can be the most practical and effective means to offer the energy demand on the earth. Producing power from RES is not only completely environmentally friendly but also reliable and renewable. Both wind and PV energies can be considered the most mature technology to produce large electric power from RES. Due to the random characteristics of RES, ESS should be effectively used to compensate for the intermittent power-generation features of RES.

Jing et al. [1] reviewed and discussed the developments of the HESS based on battery and SC used in autonomous microgrids while this study also explored both technical complexity and economic sustainability of the microgrid. Manandhar et al. [2] proposed a new control scheme for a PV-based DC grid system using an HESS with battery and SC while the control scheme employed the uncompensated power from the battery to promote the operating characteristics of the overall HESS. Lin et al. [3] proposed an integral droop (ID) to apply to a group of ESSs with high ramp rates while the transient power allocation in the HESS was able to be implemented by coordinating the ID and the traditional V-P droop. Xiao et al. [4] discussed a combined energy-storage mode to meet the ESS requirements for wind power under short-term and long-term modes, where the short-term energy-storage mode was designed to meet fast-changing powers using SCs while the long-term energy-storage mode was scheduled to meet large-scale capacity requirements using a battery based on Li-ion or VRFB. Kollimalla et al. [5] proposed a new control scheme to achieve power-sharing between batteries and SCs to match generation-demand mismatch and control grid voltage. Wang et al. [6] proposed a rule-based power-control algorithm to activate the power dispatch of a utility-scale PV power plant with a HESS according to Australian National Electricity Rules. Li et al. [7] discussed the strategies to conquer the obstacles of real-time simulations of WFs with complicated and high-frequency switching using real-time hardware-in-the-loop while a wind-turbine generator (WTG) using a HESS based on flow battery and SC to smooth wind power was investigated. Wang et al. [8] proposed a HESS consisting of a VRFB and an SC bank for smoothing the fluctuating output power of a 1-MW grid-tied PV power plant while the HESS was designed to minimize the required power rating of the SC bank to only 1/5 of the VRFB rating to avoid the VRFB operating at low power levels by increasing its overall efficiency. Manandhar et al. [9] proposed a new energy management

scheme to achieve effective power sharing between different ESSs, faster response DC-link voltage regulation, dynamic power sharing between the battery and the grid based on the battery's state of charge (SOC), etc. Samosir and Yatim [10] presented a power converter for connecting an ultracapacitor as a secondary ESS to a fuel cell while a bidirectional DC/DC converter was utilized for interfacing the ultracapacitor to the fuel cell. Wee et al. [11] used a statistical method to design a battery/SC-based ESS for a WF by treating the input wind power as random and using a proposed coordinated power flow control scheme for the ESS. Hajizadeh et al. [12] presented the control of hybrid fuel cell/energy-storage distributed generation systems subject to a voltage sag at distribution systems. Tang et al. [13] presented a coordinated optimization control scheme for a HESS based on real-time online analysis of the power spectrum while the developed device was applied to some engineering projects with both simulation and practical applications. Hazra and Bhattacharya [14] proposed a HESS comprising an ultracapacitor and battery for smoothing the oscillating power of a wave-energy conversion system while each component of the proposed HESS was sized to optimize the cost. Pan et al. [15] introduced an integrated control strategy of smoothing power fluctuations and peak shaving based on a HESS with SC and battery while the power fluctuations of the wind/PV/HESS were controlled under constraints by a low-pass filter. Wang and Yue [16] proposed a probabilistic scheme for determining the rated power capacity of a HESS while the scheme allowed for optimization of the performance of the high energy density of the battery and the SC.

This paper's contribution is to propose a scheme to design the rated powers for the VRFB and the SC of the proposed HESS to effectively stabilize the MMPS connected with a large-scale HWPF. The organization of this paper is listed below. Section 2 describes the system configuration and the associated mathematical models and/or equations of each subsystem. Section 3 depicts the design of the rated powers for the VRFB and the SC of the proposed HESS. Section 4 demonstrates the calculated eigenvalues and root-loci plots for small-signal stability analysis of the studied system. Section 5 illustrates dynamic and transient time-domain simulations of the studied system under variable wind speeds and solar irradiations as well as sudden trips of PV farm and WF. The important specific conclusions are depicted in Section 6.

2 Architecture of the studied system and mathematical models

Figure 1 shows the one-line architecture of the studied system, where the HWPF of rated 100 MW consists of an equivalently aggregated PV farm of rated 25 MW

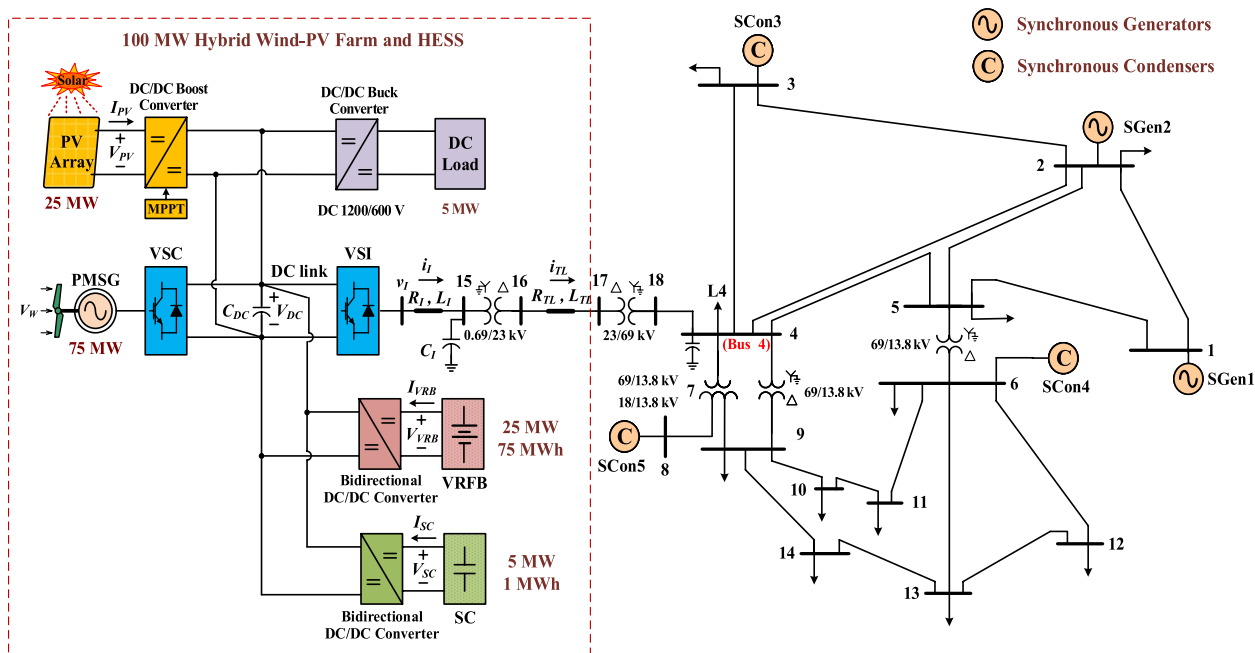


Fig. 1 Architecture of the studied MMPS connected with a large-scale HWPF through the proposed HESS [17, 19]

and an equivalently aggregated WF based on a permanent-magnet synchronous generator (PMSG) of rated 75 MW. The common DC link of rated 1200 V is connected to the WF, the PV farm, an equivalently aggregated DC load, and a HESS through an equivalently aggregated AC/DC voltage-source converter (VSC), an equivalently aggregated DC/DC boost converter, an equivalently aggregated DC/DC buck converter, and two equivalently aggregated bidirectional DC/DC converter, respectively. The common DC link of rated 1200 V is also connected to Bus 4 of the 14-bus MMPS [17] through an equivalently aggregated bidirectional DC/AC voltage-source inverter (VSI), two step-up power transformers, and a power cable. Bus 4 shown in Fig. 1 can be treated as the point of common coupling (PCC) where the HWPF is linked to the MMPS. This paper refers to the models of the 1200-V DC link, the PV array with the DC/DC boost converter, the SC bank with the bidirectional DC/DC converter, and other subsystems shown in [18] to develop a new system architecture shown in Fig. 1 with the HWPF, the HESS, the MMPS, etc.

Bus 4 shown in Fig. 1 is a very important bus to accept large power fluctuations generated from the HWPF of rated 100 MW. Such large time-varying injected power into Bus 4 can cause large voltage variations on Bus 4 and neighboring buses. Hence, the proposed HESS in this paper is used to effectively mitigate and smooth such power fluctuations injected into Bus 4.

2.1 Controls of the AC/DC VSC of the WF

The control block diagram of the equivalently aggregated AC/DC VSC of the WF based on PMSG is illustrated in Fig. 2. The major goal of this control block diagram is that the WF can capture available maximum power from variable wind speeds. To achieve this purpose, the optimal torque control algorithm [18, 20, 21] of the wind PMSG can be embedded in the control program of the AC/DC VSC. The cut-in, rated, and cut-out wind speeds of the wind turbine of the WF are appropriately chosen as 4, 12, and 24 m s⁻¹, respectively.

2.2 Models of the PV farm and its DC/DC boost converter

The single-diode equivalent-circuit model of a PV cell is shown in Fig. 3, [18, 22, 23], which can be extended to establish the model of a PV farm by using the scheme presented in [18]. The schematic diagram of the DC/DC boost converter for connecting the output of the PV farm to the common DC link of rated 1200 V is shown in Fig. 4. The mathematical equations associated with the dynamic average-value model of the DC/DC boost converter shown in Fig. 4 can be referred to [18].

2.3 Models of the bidirectional DC/DC converter and the HESS

The equivalent circuit diagram of the bidirectional DC/DC converter for integrating the energy-storage unit into the common DC link of rated 1200 V is shown in Fig. 5. The two power semiconductor switches S_1 and S_2 of the bidirectional

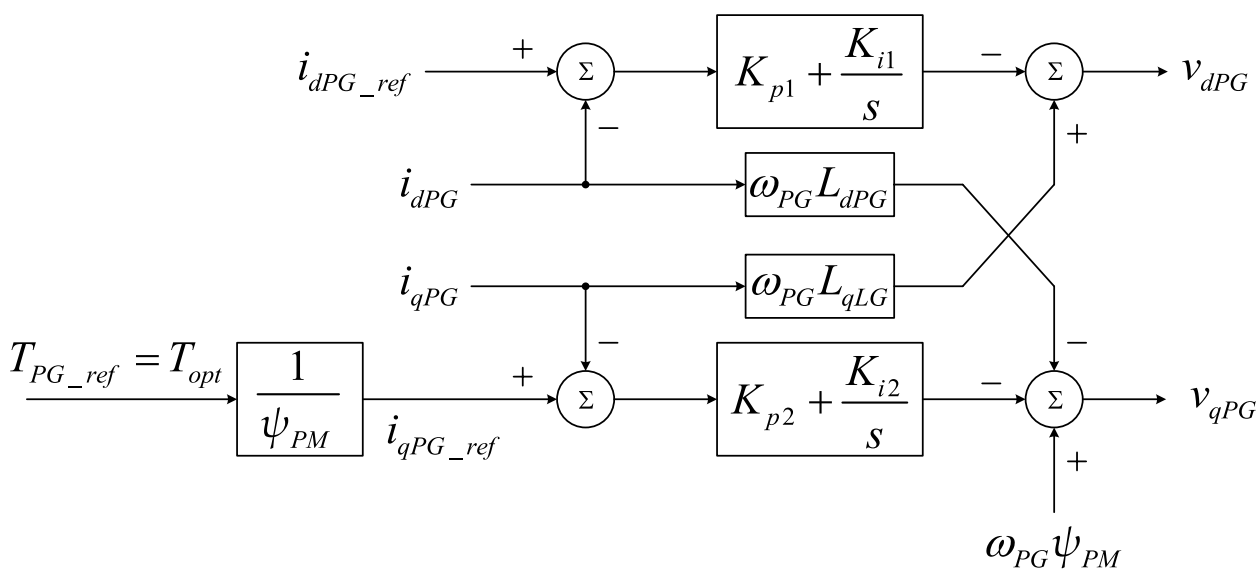


Fig. 2 Control block diagram of the AC/DC VSC of the wind PMSG

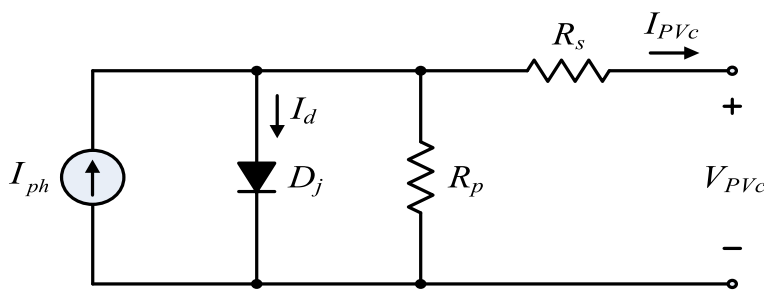


Fig. 3 Single-diode equivalent-circuit model of the PV cell

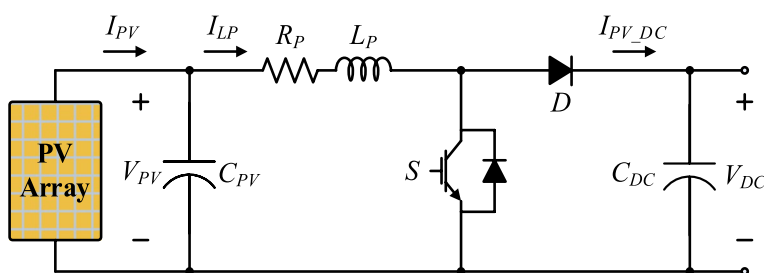


Fig. 4 Schematic diagram of the DC/DC boost converter connected to the output of the PV array

DC/DC converter are operated in a complementary manner [10, 18] and, thus, this converter can operate either as a buck converter (buck mode) or a boost converter (boost mode). The level of the power loss of the two power semiconductor switches S_1 and S_2 of the bidirectional DC/DC converter is around 500–600 W. It is assumed that the two power semiconductor switches S_1 and S_2 can properly neglect their power losses while the bidirectional DC/DC converter can be simulated by using its dynamic average-value model [18].

The equivalent circuit model of the employed VRFB-based ESS is shown in Fig. 6, where the resistance R_{fix} represents the parasitic loss, the resistances R_{rea} and R_{res} denote the internal losses, and I_{VRFB} , I_{sta} , and I_{pump} stand for the output current, the stack current, and the pump current, respectively. The equivalent-circuit model of the employed SC is shown in Fig. 7, where the capacitance C_{SC} , the parallel resistance R_{pSC} , and the series resistance R_{sSC} are used [10].

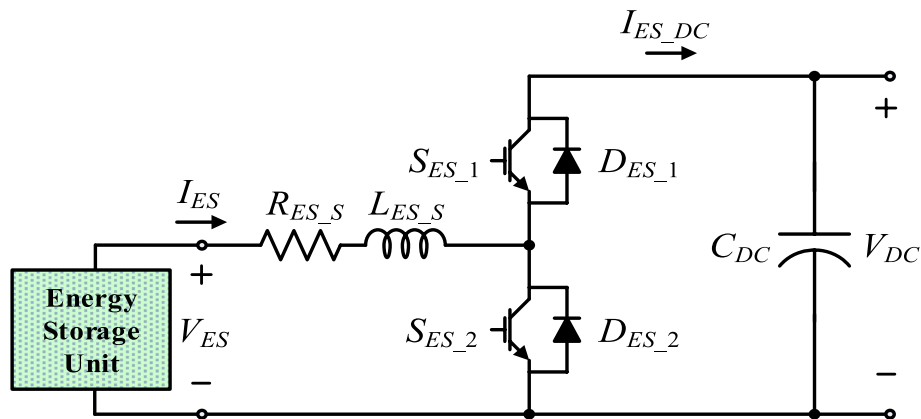


Fig. 5 Schematic diagram of the bidirectional DC/DC converter for integrating an energy-storage unit into the common DC link

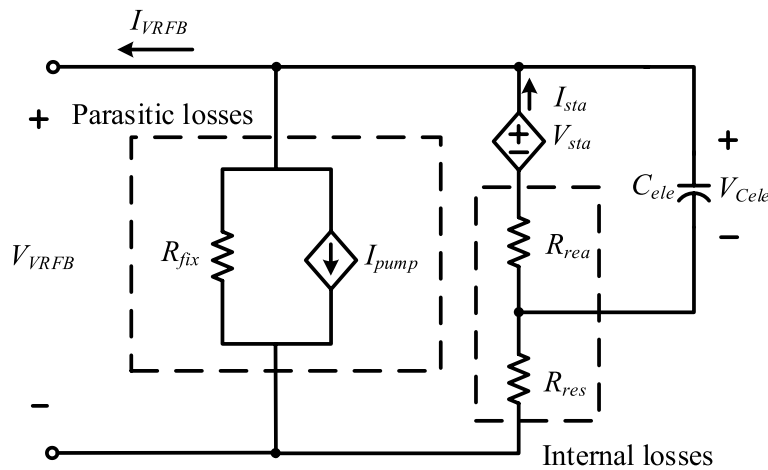


Fig. 6 Equivalent-circuit model of the studied VRFB

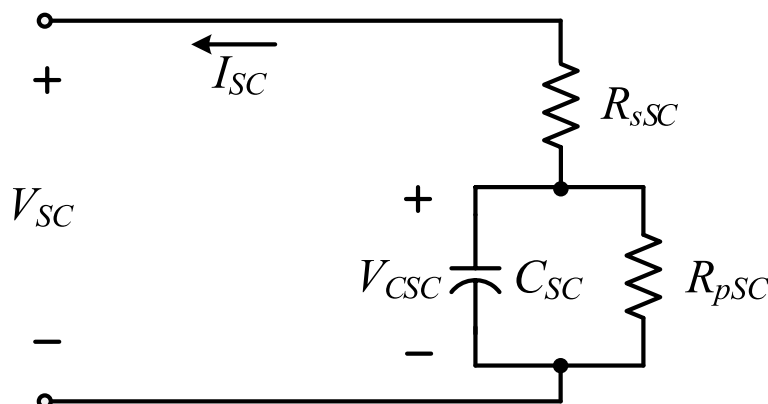


Fig. 7 Equivalent-circuit model of the studied SC

2.4 Controls of the DC/AC VSI

The control block diagram of the DC/AC VSI is shown in Fig. 8. The purpose of the DC/AC VSI is to keep the

DC-link voltage V_{DC} at its reference value of V_{DC_ref} and control the reactive power to exchange with the AC system. To achieve the decoupled control between the

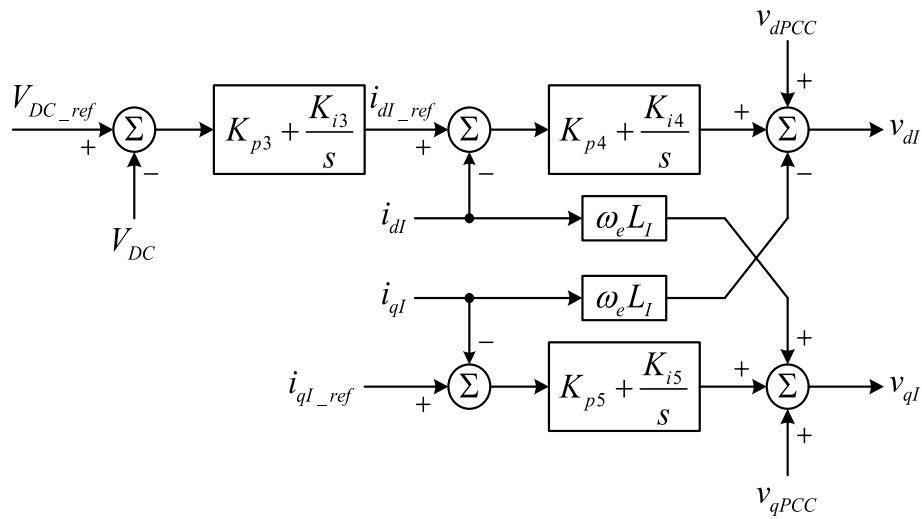


Fig. 8 Control block diagram of the studied DC/AC VSI

active and reactive components, the dq -axis reference frame with the d -axis aligned with the voltage vector of Bus 15 shown in Fig. 1 is used. Thus, the d - and q -axis currents of the VSI (i_{dl} and i_{ql}) are employed to control the DC-link voltage and the reactive power that the VSI exchanges with the AC grid, respectively.

2.5 Controls of the HESS

The control block diagram of the proposed HESS is shown in Fig. 9. The main target of this control block is to smooth the output power of the HWPF. To take the average output active powers of the two farms and compare them with the actual current active powers, the total power reference of P_{Tot_ref} can be obtained by measuring the active powers of the WF and the PV farm fed into the common DC link. When the signal P_{Tot_ref} passes through the low-pass filter, the output power reference of the VRFB (P_{VRFB_ref}) can be obtained. By subtracting P_{Tot_ref} from P_{VRFB_ref} the high-frequency power components (P_{Tran}) yield. When the output power error of the VRFB

(P_{VRFB_err}) passes through the ratio of the two voltages and adds up P_{Tran} , the output power reference of the SC (P_{SC_ref}) can be determined.

3 Rated power design of the HESS

To determine the rated power of the HESS to smooth the total output power fluctuations of the HWPF, the employed dynamic output powers of the WF and the PV farm are shown in Fig. 10a and b, respectively. Figure 11 shows the dynamic results of the total power reference (P_{Tot_ref}) required by the HESS. It can be discovered that the output active powers of the WF and the PV farm are fast changing while the actual wind power drops rapidly from 6 to 8 d. To effectively smooth power fluctuations, the HESS must output the required smoothing power P_{Tot_ref} when the system power demand suddenly rises. To directly observe the frequency of the peak occurrence of P_{Tot_ref} the bar diagram shown in Fig. 12 is used to explain the dynamic response simulations of P_{Tot_ref} shown in Fig. 11. The

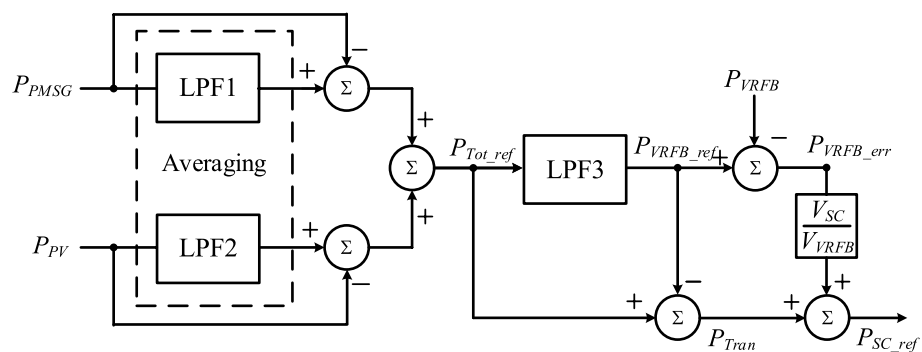


Fig. 9 Control block diagram of the proposed HESS

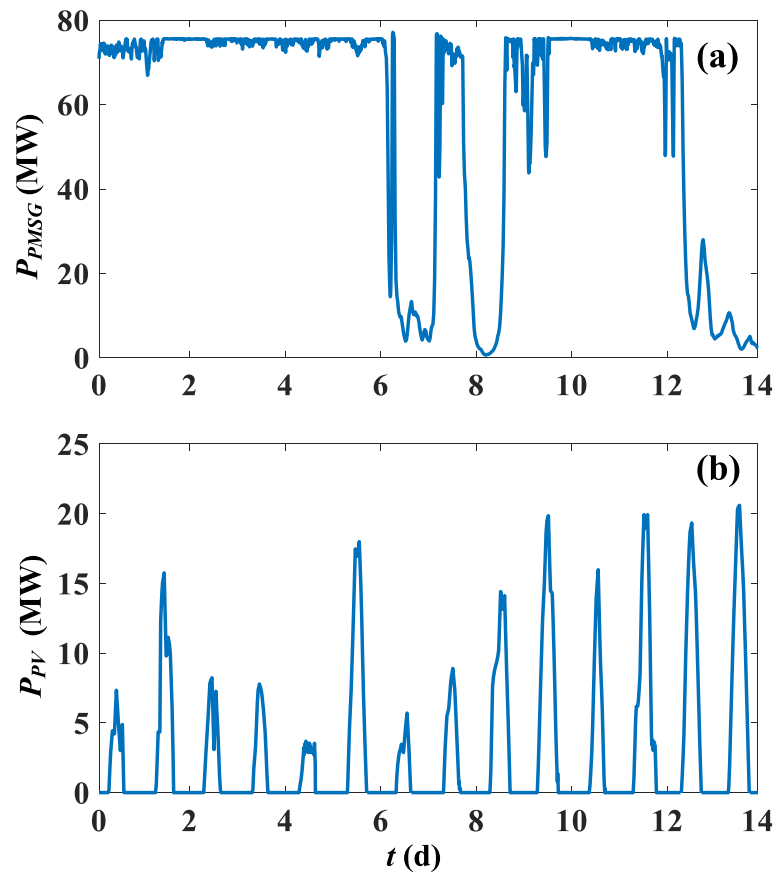


Fig. 10 Dynamic responses of the studied system subject to actual wind variations and actual solar irradiance variations. **a** P_{PMSG} (MW) **b** P_{PV} (MW)

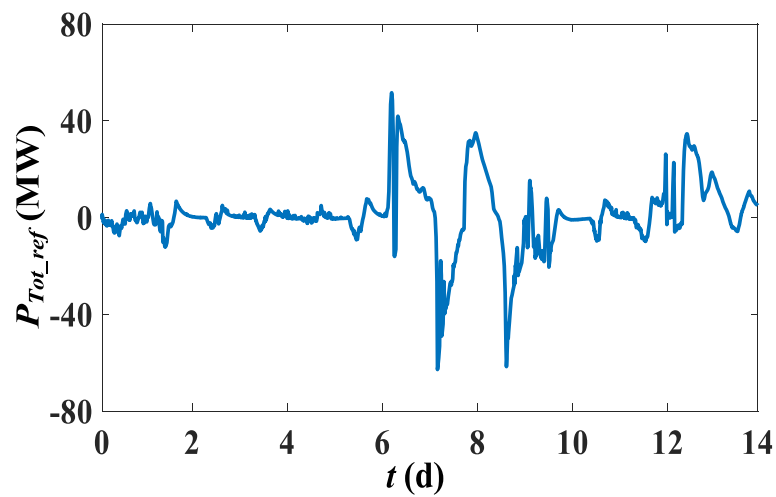


Fig. 11 Dynamic responses of P_{Tot_ref}

horizontal coordinate in Fig. 12 represents all the total power smoothing reference absolute value $|P_{Tot_ref}|$ that may occur while the vertical coordinate in Fig. 12 represents the numbers of occurrence of $|P_{Tot_ref}|$ in

all data. It can be observed from the results shown in Fig. 12 that the occurrence of the peak values of $|P_{Tot_ref}|$ is very low when compared to the lower value of $|P_{Tot_ref}|$.

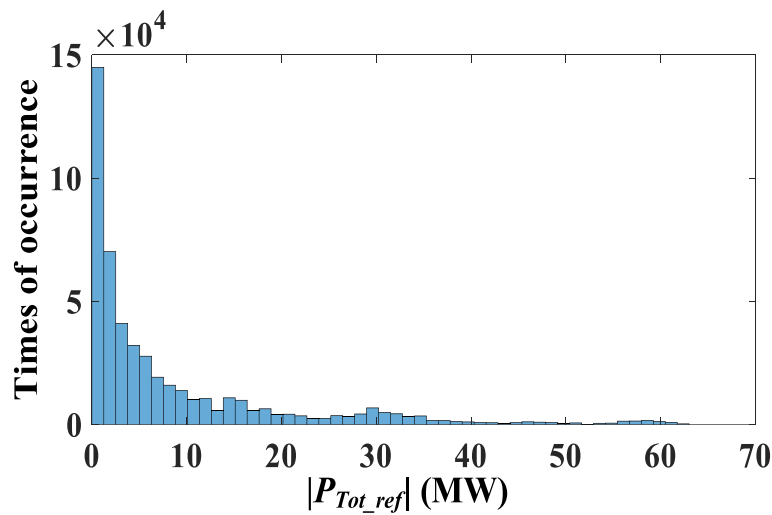


Fig. 12 Bar diagram of $|P_{Tot_ref}|$

Applying the Kernel smoothing density estimation (KSDE) [16] to the bar diagram shown in Fig. 12, the probability density function (PDF) results of $|P_{Tot_ref}|$ can be obtained. The function is expressed below.

$$[\phi_{HESS}, |P_{Tot_ref}|_i] = KSDE(|P_{Tot_ref}|) \tag{1}$$

where $|P_{Tot_ref}|_i$ represents the selected vector of 100 points equally spaced in the range of $|P_{Tot_ref}|$ and ϕ_{HESS} represents the vector of KSDE corresponding to absolute values. This is theoretically optimal for estimating the density with a normal distribution.

Figure 13 shows the PDF results of $|P_{Tot_ref}|$, where the horizontal coordinate represents the power of $|P_{Tot_ref}|$ while the vertical coordinate represents the probability density of the power in all data. It can be clearly observed the probability of occurrence of $|P_{Tot_ref}|$ that most $|P_{Tot_ref}|$ results almost distribute between 0 and 30 MW

while the probability of occurrence of $|P_{Tot_ref}|$ over 30 MW is very low. The following will use the cumulative density function (CDF) for the PDF results of $|P_{Tot_ref}|$ obtained in Fig. 13.

According to Fig. 13 for the PDF of $|P_{Tot_ref}|$ obtained, the CDF results of $|P_{Tot_ref}|$ can be found below.

$$F(x) = \int_0^x \phi_{HESS}(|P_{Tot_ref}|)d(|P_{Tot_ref}|) \tag{2}$$

where ϕ_{HESS} is the function of variables and $F(x)$ is integral of the function. The CDF results of $|P_{Tot_ref}|$ shown in Fig. 14 are calculated by using Eq. (2), where the horizontal coordinate represents the occurrence of all data of $|P_{Tot_ref}|$, the vertical coordinate represents the probability density currently accumulated in all data, and the sum of the last accumulated probability must be equal to 1.

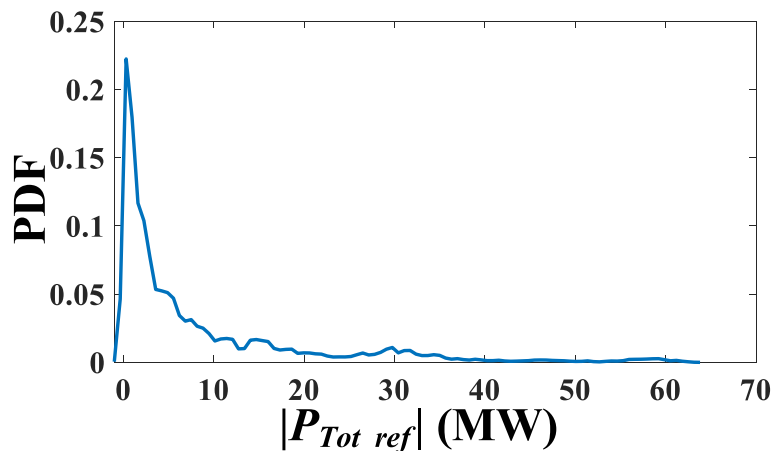


Fig. 13 Probability density function (PDF) results of $|P_{Tot_ref}|$

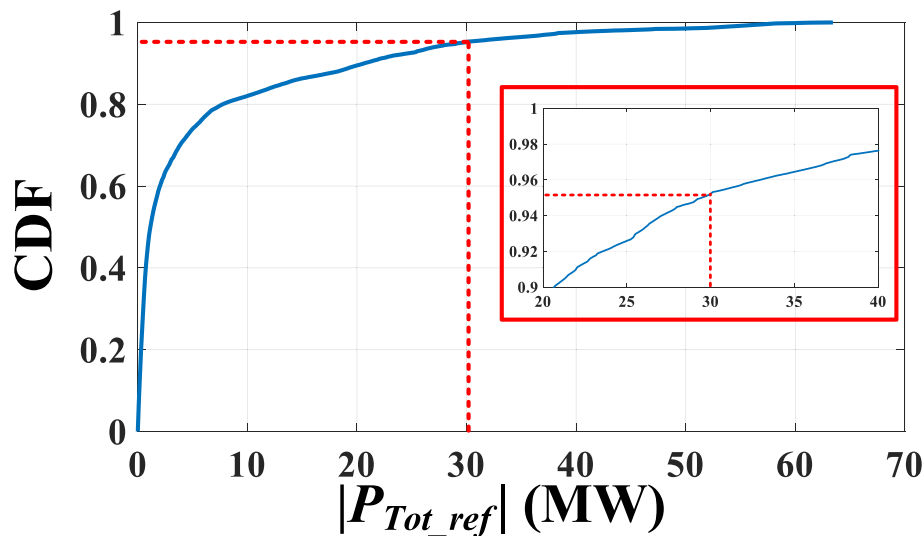


Fig. 14 Cumulative density function (CDF) results of $|P_{Tot_ref}|$

Figure 15 illustrates the characteristic curves of discharge efficiency versus output power of the VRFB-ESS when the values of the state of charge (SOC) of the VRFB-ESS are 20, 50, and 80%. It can be observed that the discharge efficiency of the VRFB-ESS remains at a higher position with higher SOC and higher output power. When the output power of the VRFB-ESS is less than 20% of its rated power, its discharge efficiency drops rapidly to be lower than 75%. Hence, the rated power of the SC-ESS will be selected to be 20% of the one of the VRFB-ESS. This configuration can enable SC-ESS to share the pressure of the VRFB-ESS and reduce the impacts of the VRFB-ESS subject to the variable output power of the HWPF. When the output

power of the VRFB-ESS is lower than 20% of its rated power, the addition of the SC-ESS can keep the VRFB-ESS running at a higher efficiency. Therefore, the rated power of the VRFB-ESS is designed to be 25 MW and the rated power of the SC-ESS is selected to be 5 MW.

4 Small-signal stability analysis

4.1 System eigenvalues

In this paper, the wind speed of 11 m s^{-1} and the solar irradiance of 950 W m^{-2} are properly selected as the nominal operating conditions for the WF and the PV farm, respectively. The system eigenvalues of the studied system without ESS, with VRFB-ESS only, with SC-ESS only, and with the HESS under the selected nominal

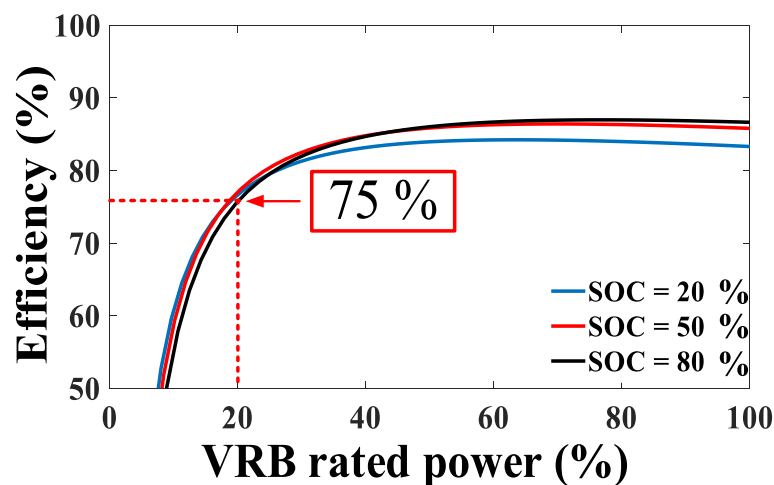


Fig. 15 Characteristic curves of discharge efficiency versus output power of the studied VRFB

operating conditions are listed in Table 1. In Table 1, the eigenvalues $\Lambda_1-\Lambda_{29}$, $\Lambda_{30}-\Lambda_{36}$, $\Lambda_{37}-\Lambda_{38}$, $\Lambda_{39}-\Lambda_{40}$, $\Lambda_{41}-\Lambda_{52}$ and $\Lambda_{53}-\Lambda_{59}$ dominant the electromechanical modes of the synchronous generators of the MMPS, the modes of the PMSG-based WF with its AC/DC VSC, the modes of the PV farm with its DC/DC boost converter, the modes of the DC load with its DC/DC buck converter, the modes of the bidirectional DC/AC VSI with its common DC link, and the modes of the VRFB-ESS, the SC-ESS, and their bidirectional DC/DC converters, respectively.

When the VRFB-ESS, the SC-ESS, and the HESS are in service, respectively, it is seen from Table 1 that the real parts of the modes $\Lambda_{41}-\Lambda_{52}$ move rightward toward the imaginary axis of the complex plane. Because both VRFB-ESS and SC-ESS are operated at “trickle charge” mode under steady-state conditions, they are equivalent to two electrical loads to absorb power from the common DC link. Therefore, the bidirectional DC/AC VSI with its

common DC link has significant influences on the overall system stability to maintain stable operating conditions.

4.2 Root-loci analysis

When the wind speed of the WF increases from 4 to 12 m s⁻¹ and the solar irradiance of the PV farm keeps at 950 W m⁻², the root-loci plots of some specified modes of the studied system are shown in Fig. 16. It can be discovered that the root-loci plots of the modes $\Lambda_{45}-\Lambda_{46}$ for the common DC-link voltage move further away from the imaginary axis of the complex plane. When the wind speed of the WF exceeds the rated wind speed of 12 m s⁻¹ of the wind turbine, the pitch angle control system of the wind turbine activates and the output active power of the WF keeps constant. Hence, when the wind speed increases from 13 to 15 m s⁻¹, the root loci of the modes $\Lambda_{45}-\Lambda_{46}$ are identical. When the VRFB-ESS, the SC-ESS, and the HESS are in service, respectively, the root-loci

Table 1 Eigenvalues (rad s⁻¹) of the studied system under the selected wind speed of 11 m s⁻¹ and the solar irradiance of 950 W m⁻²

Mode	System without ESS	System with VRFB-ESS	System with SC-ESS	System with HESS
Λ_{1-2} EM modes of 14-bus multimachine power system	-1.56 ± j14.81	-1.56 ± j14.81	-1.56 ± j14.81	-1.56 ± j14.81
Λ_{3-4}	-1.84 ± j7.91	-1.84 ± j7.91	-1.84 ± j7.91	-1.84 ± j7.91
Λ_{5-6}	-0.93 ± j12.31	-0.93 ± j12.31	-0.93 ± j12.31	-0.93 ± j12.31
Λ_{7-8}	-0.82 ± j10.56	-0.82 ± j10.56	-0.82 ± j10.56	-0.82 ± j10.56
Λ_{9-10} Other modes of 14-bus multimachine power system	-1.17 ± j0.67	-1.17 ± j0.67	-1.17 ± j0.67	-1.17 ± j0.67
Λ_{11-12}	-1.35 ± j0.29	-1.35 ± j0.29	-1.35 ± j0.29	-1.35 ± j0.29
Λ_{13-14}	-1.06 ± j0.29	-1.06 ± j0.29	-1.06 ± j0.29	-1.06 ± j0.29
Λ_{15-16}	-0.844 ± j0.19	-0.84 ± j0.19	-0.84 ± j0.19	-0.84 ± j0.19
Λ_{17-18}	-0.49 ± j0.37	-0.49 ± j0.37	-0.49 ± j0.37	-0.49 ± j0.37
Λ_{19-20}	-3.87 ± j0.82	-3.87 ± j0.82	-3.87 ± j0.82	-3.87 ± j0.82
Λ_{21-22}	-2.06 ± j0.26	-2.06 ± j0.26	-2.06 ± j0.26	-2.06 ± j0.26
Λ_{23-24}	-0.26, -1.02	-0.26, -1.02	-0.26, 1.02	-0.26, -1.02
Λ_{25-26}	-1.06, -1.80	-1.06, -1.80	-1.06, -1.80	-1.06, -1.80
Λ_{27-28}	-10.95, -16.19	-10.95, -16.19	-10.95, -16.19	-10.95, -16.19
Λ_{29}	-16.91	-16.91	-16.91	-16.91
Λ_{30-31} WTG with its AC/DC VSC of the WF	-5.30 ± j13.84	-5.30 ± j13.84	-5.30 ± j13.84	-5.30 ± j13.84
Λ_{32}	-0.46	-0.46	-0.46	-0.46
Λ_{33-34}	-201.3, -200.0	-201.3, -200.0	-201.3, -200.0	-201.3, -200.0
Λ_{35-36}	-490.2 ± j191.0	-488.8 ± j185.3	-487.1 ± j183.1	-486.9 ± j183.3
Λ_{37-38} PV farm	-1316.5 ± j498.1	-1322.2 ± j504.5	-1322.5 ± j504.6	-1322.4 ± j504.5
Λ_{39-40} DC load	-0.58 ± j2295.6	-0.52 ± j2276.7	-0.55 ± j2276.8	-0.49 ± j2276.8
Λ_{41-42} DC/AC VSI with its common DC link	-741.4 ± j636.7	-740.0 ± j631.5	-740.3 ± j631.2	-739.7 ± j631.4
Λ_{43-44}	-4.11 ± j4.33	-4.11 ± j4.33	-4.11 ± j4.33	-4.11 ± j4.33
Λ_{45-46}	-155.1 ± j353.9	-148.4 ± j354.6	-149.1 ± j354.2	-147.8 ± j354.9
Λ_{47-48}	-258.9 ± j7649.1	-258.8 ± j7649.0	-258.8 ± j7649.0	-258.8 ± j7649.0
Λ_{49-50}	-896.0 ± j6287.3	-896.9 ± j6287.2	-896.0 ± j6287.2	-896.0 ± j6287.2
Λ_{51-52}	-203.6 ± j105.6	-201.5 ± j104.4	-201.9 ± j104.7	-201.4 ± j104.6
Λ_{53-54} VRFB-ESS and SC-ESS	-	-0.02, -0.04	-0.02, -0.04	-0.02, -0.04
Λ_{55-56}	-	-472.31, -0.167	-	-517.88, -0.16
Λ_{57-58}	-	-1139.7	-1143.5	-1139.87, -1143.57
Λ_{59}	-	-	-105.67	-102.45

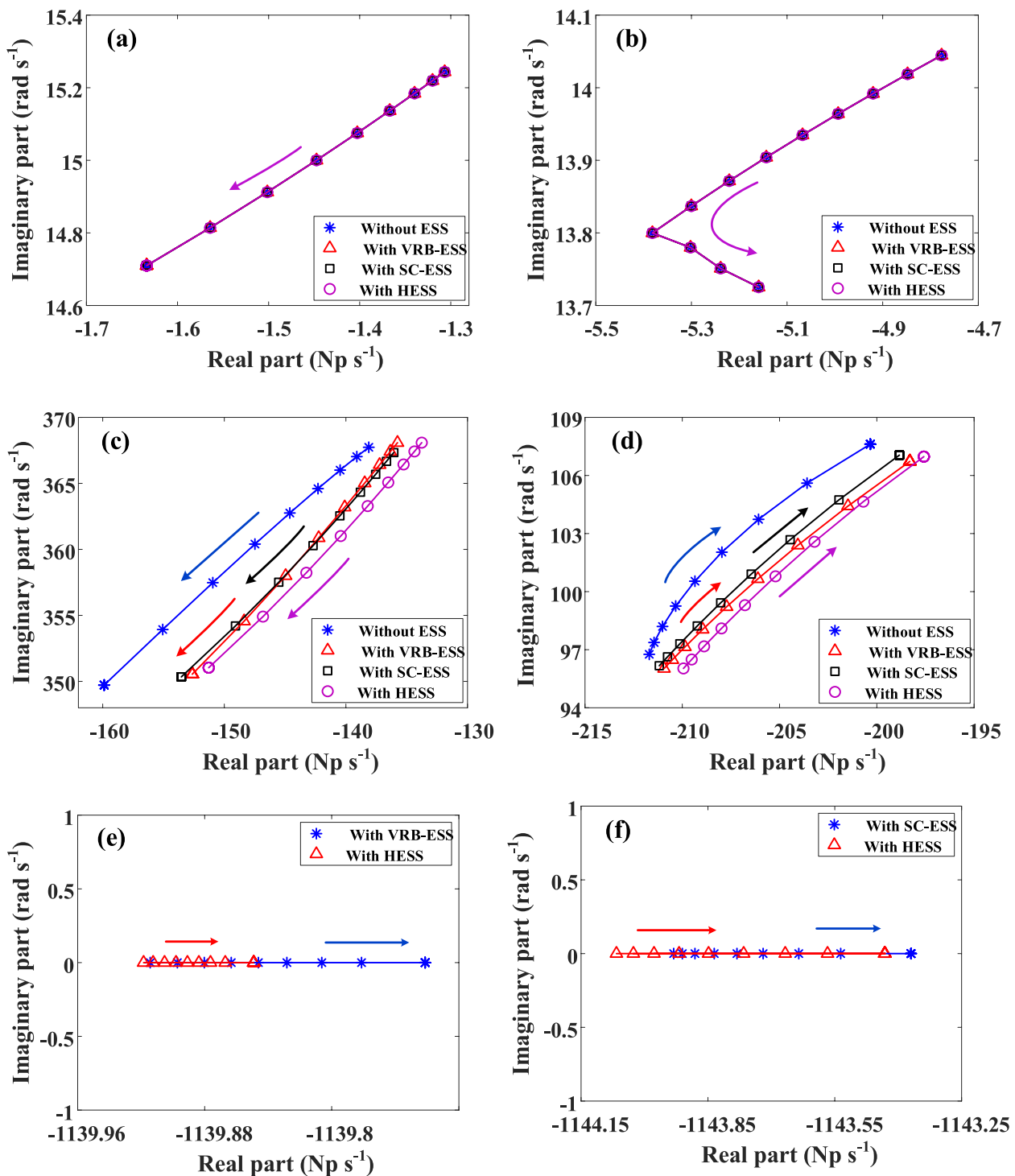


Fig. 16 Root-loci plots of the dominant modes of the system eigenvalues when the wind speed V_w of the WF increases from 4 to 15 m s^{-1} and the solar irradiance of the PV farm keeps at 950 W m^{-2} . **a** Λ_{1-2} **b** Λ_{30-31} **c** Λ_{45-46} **d** Λ_{51-52} **e** Λ_{57} **f** Λ_{58}

plots of the modes $\Lambda_{45}-\Lambda_{46}$ move toward the imaginary axis of the complex plane. This is because these ESSs are operated as electrical loads under steady-state conditions, and the studied system can still maintain stable operation.

When the solar irradiance of the PV farm increases from 10^2 to 10^3 W m^{-2} and the wind speed of the WF keeps at 11 m s^{-1} , the root-loci plots of the studied system are shown in Fig. 17. With the increase of solar

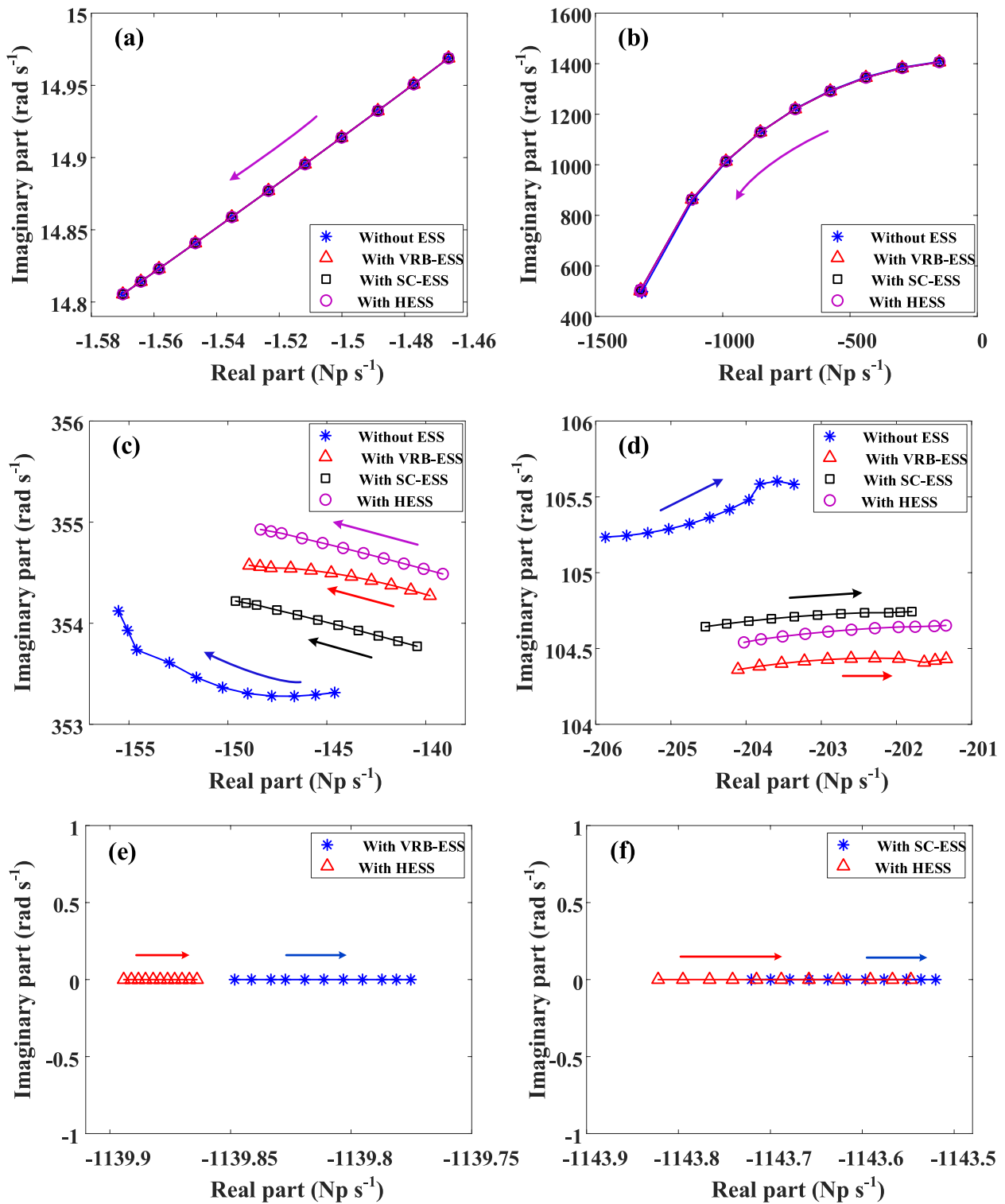


Fig. 17 Root-loci plots of the dominant modes of the system eigenvalues when the solar irradiance G of the PV farm increases from 100 to 1000 $W m^{-2}$ and the wind speed of the WF keeps at $11 m s^{-1}$. **a** Λ_{1-2} **b** Λ_{37-38} **c** Λ_{45-46} **d** Λ_{51-52} **e** Λ_{57} **f** Λ_{58}

irradiance, the output active power of the HWPF also increases and the root-loci plots of the modes Λ_{45-46} for the common DC-link voltage move further away from the imaginary axis of the complex plane. When the VRFB-ESS, the SC-ESS, and the HESS are in service, respectively, the root-loci plots of the modes Λ_{45-46} for the common DC-link voltage move closer to the imaginary axis of the complex plane to make the studied system stable operation.

Figure 16c and d show the root-loci plots of the modes Λ_{45-46} and Λ_{51-52} under different values of wind speed, respectively. It can be found in Fig. 16c and d that the modes Λ_{45-46} and Λ_{51-52} of the studied system without ESS have the largest root-loci variations on their real parts while the modes Λ_{45-46} and Λ_{51-52} of the studied system with different ESSs have smaller root-loci variations on their real parts. The differences between the root-loci variations on the real parts of the modes Λ_{45-46} and Λ_{51-52} of the studied system with different ESSs and without ESS are the quantitative indicators related to stability improvement of using the different ESSs.

Similar situations can also be observed in Fig. 17c and d. Figure 17c and d illustrate the root-loci plots of the modes Λ_{45-46} and Λ_{51-52} under different values of solar irradiance, respectively. It can be found in Fig. 17c and d that the modes Λ_{45-46} and Λ_{51-52} of the studied system without ESS have the largest root-loci variations on their real parts while the modes Λ_{45-46} and Λ_{51-52} of the studied system with different ESSs have smaller root-loci variations on their real parts. The differences between the root-loci variations on the real parts of the modes Λ_{45-46} and Λ_{51-52} of the studied system with different ESSs and without ESS are also the quantitative indicators related to stability improvement of using the different ESSs.

5 Time-domain simulations

5.1 Simulated variable wind speeds and simulated variable solar irradiances simultaneously applied to the HWPF

When the simulated variable wind speeds and the simulated variable solar irradiances are simultaneously applied to the HWPF, the dynamic time-domain simulations are shown in Fig. 18. When only the VRFB-ESS is in service, the total active power flowing into PCC (P_{Bus4}) has been smoothly improved. However, during the two-time intervals of $t=40-60$ s and $t=85-90$ s, the output active power of the VRFB-ESS reaches its rated power's upper limit and, hence, the smoothing effect of the VRFB-ESS on the total active power input to PCC will be lost. When the HESS is in service, it can be observed that the total active power flowing into PCC can be effectively smoothed during the two-time intervals of $t=40-60$ s and $t=85-90$ s.

5.2 Actual wind-speed variations and actual solar irradiance variations simultaneously applied to the HWPF

When the actual wind speeds and the actual solar irradiances are simultaneously applied to the HWPF, the dynamic time-domain simulations are shown in Fig. 19. When only the VRFB-ESS is in service, the total active power flowing into PCC has been obviously smoothed. However, the active-power fluctuations of the HWPF are too large during the time interval from 6 to 8 d since the active-power output of the VRFB-ESS reaches its rated power's upper limit and, hence, the obvious fluctuations of the total active power flowing into PCC can be seen. When the proposed HESS is in service, the total active power flowing into PCC can be effectively smoothed during the time interval from 6 to 8 d.

5.3 PV farm suddenly tripped

When the PV farm is suddenly tripped at $t=10$ s, the transient time-domain simulations without ESS, with only VRFB-ESS, and with the HESS under the nominal operating condition are shown in Fig. 20. It can be observed from Fig. 20c that when no ESS is in service, the active power flowing into PCC drops to as low as about 0.45 per unit (p.u.) at $t=10$ s and then reach a new operating point after the trip of the PV farm. When only the VRFB-ESS is in service, the active power flowing into PCC drops as low as about 0.59 p.u. at $t=10$ s and then slowly returns to the original operating point after 0.025 s due to the active-power compensation of the VRFB-ESS. When the HESS is in service, the same active-power compensation effect can be obtained from the HESS and the active power flowing into PCC drops as low as about 0.62 p.u. at $t=10$ s and then quickly returns to the original operating point after 0.025 s.

5.4 WF suddenly tripped

When the WF is suddenly tripped at $t=10$ s, the transient time-domain simulations without ESS, with the VRFB-ESS only, and with the HESS under the nominal operating condition are plotted in Fig. 21. It can be found from Fig. 21c that when no ESS is in service, the active power flowing into PCC drops to as low as about 0.09 p.u. and then reach a new operating point after the trip of the WF. When only the VRFB-ESS is in service, the active power flowing into PCC drops to as low as about 0.19 p.u. at $t=10$ s and then slowly returns back to the original operating point after 0.025 s. When the proposed HESS is in service, the active power flowing into PCC drops to as low as about 0.3 p.u. at $t=10$ s and then slow recoveries back to the original operating point after 0.025 s.

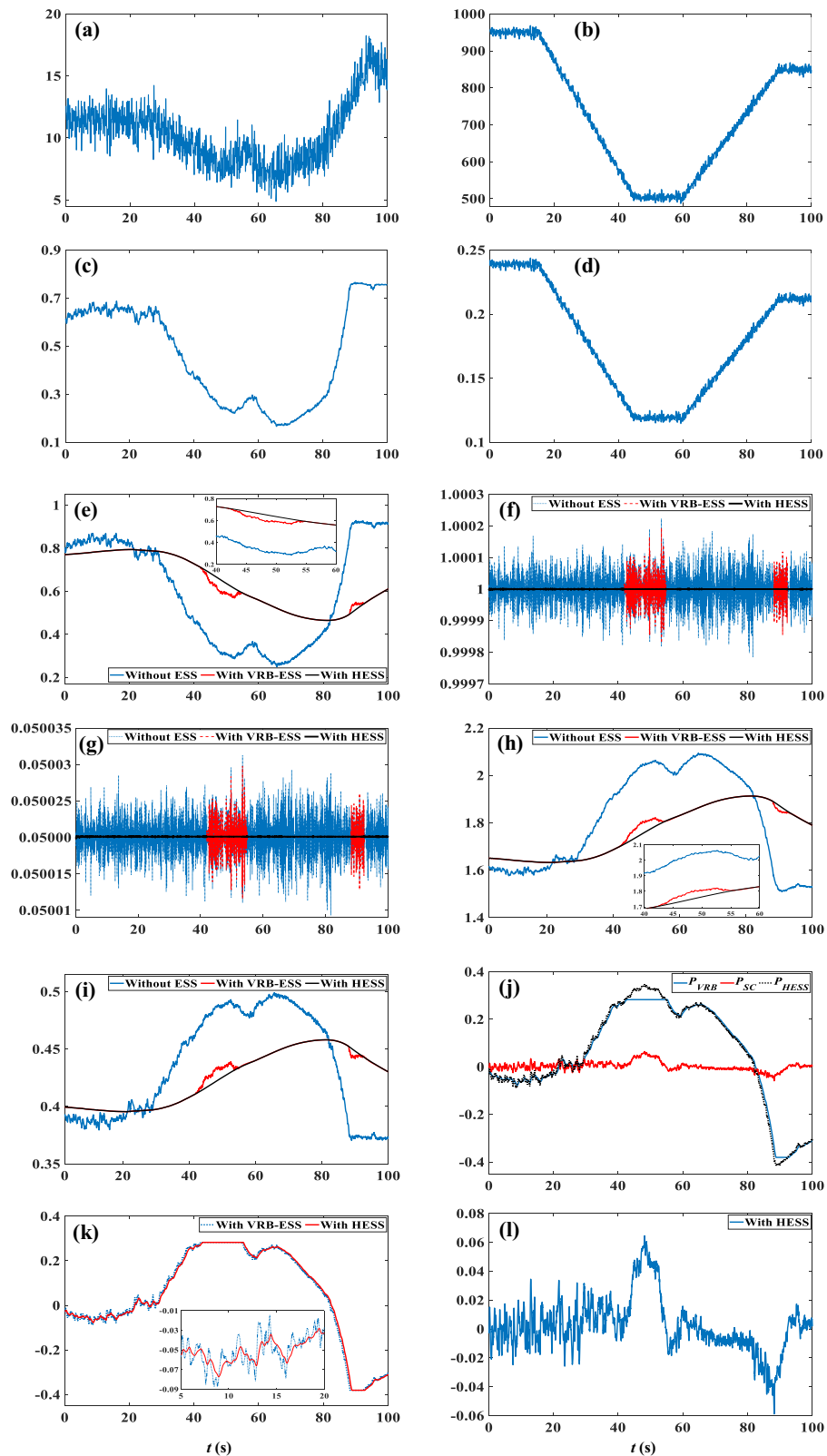


Fig. 18 Dynamic responses of the studied system subject to simulated wind-speed variations and simulated solar irradiance variations **a** V_w (m s⁻¹) **b** G (W m⁻²) **c** P_{MSG} (p.u.) **d** P_{PV} (p.u.) **e** P_{BUS4} (p.u.) **f** V_{DClink} (p.u.) **g** P_{DCload} (p.u.) **h** P_{SGen1} (p.u.) **i** P_{SGen2} (p.u.) **j** P_{HESS} (p.u.) **k** P_{VRB} (p.u.) **l** P_{SC} (p.u.)

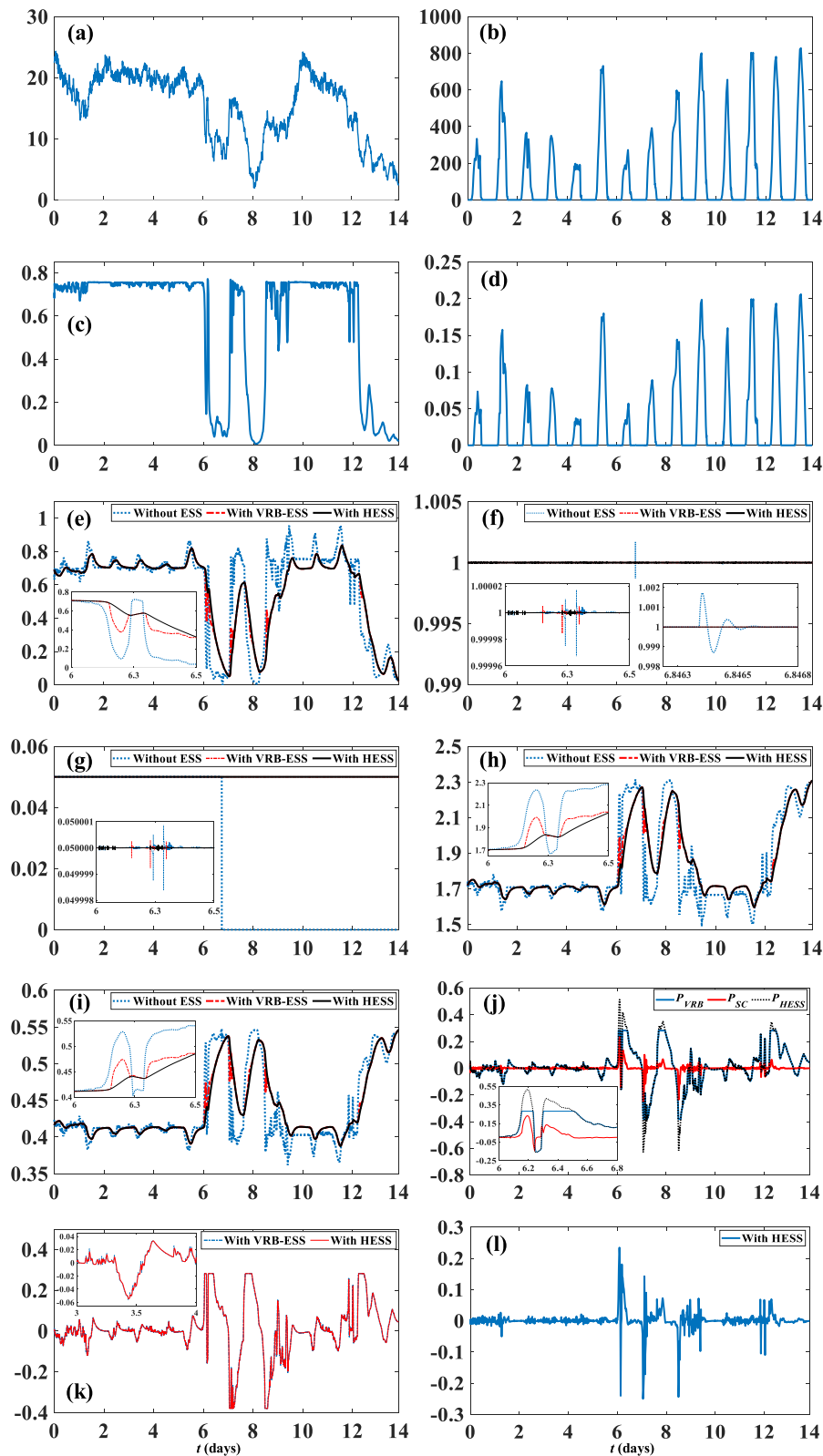


Fig. 19 Dynamic responses of the studied system subject to actual wind-speed variations and actual solar irradiance variations **a** V_w ($m s^{-1}$) **b** G ($W m^{-2}$) **c** P_{PMSG} (p.u.) **d** P_{PV} (p.u.) **e** P_{BUS4} (p.u.) **f** V_{DClink} (p.u.) **g** P_{DCload} (p.u.) **h** P_{Sgen1} (p.u.) **i** P_{Sgen2} (p.u.) **j** P_{HESS} (p.u.) **k** P_{VRB} (p.u.) **l** P_{SC} (p.u.)

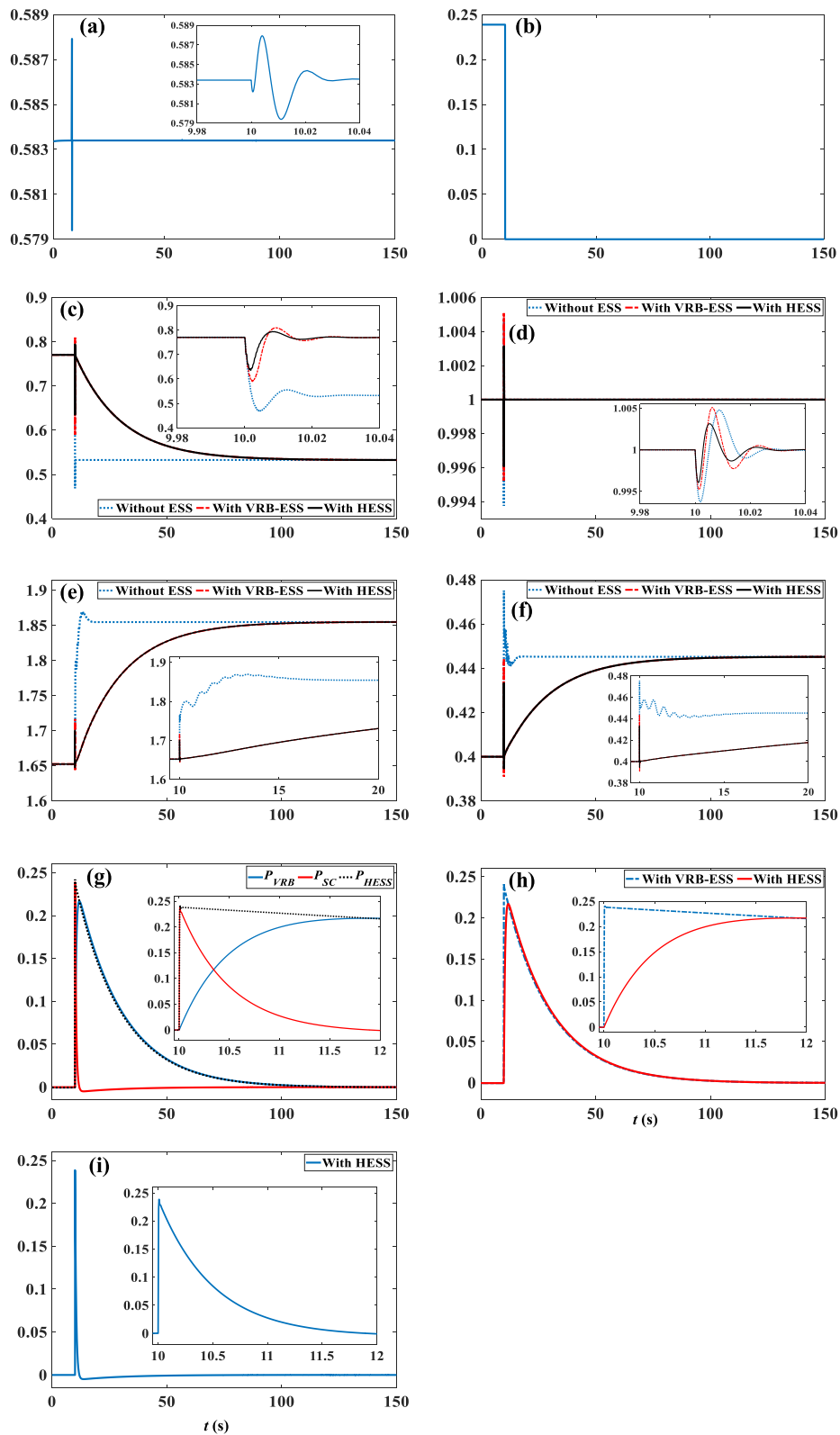


Fig. 20 Transient responses of the studied system when the studied PV farm is suddenly tripped at $t = 10$ s. **a** P_{PMSG} (p.u.) **b** P_{PV} (p.u.) **c** P_{BUS4} (p.u.) **d** $V_{DC\ link}$ (p.u.) **e** P_{SGen1} (p.u.) **f** P_{SGen2} (p.u.) **g** P_{HESS} (p.u.) **h** P_{VRB} (p.u.) **i** P_{SC} (p.u.)

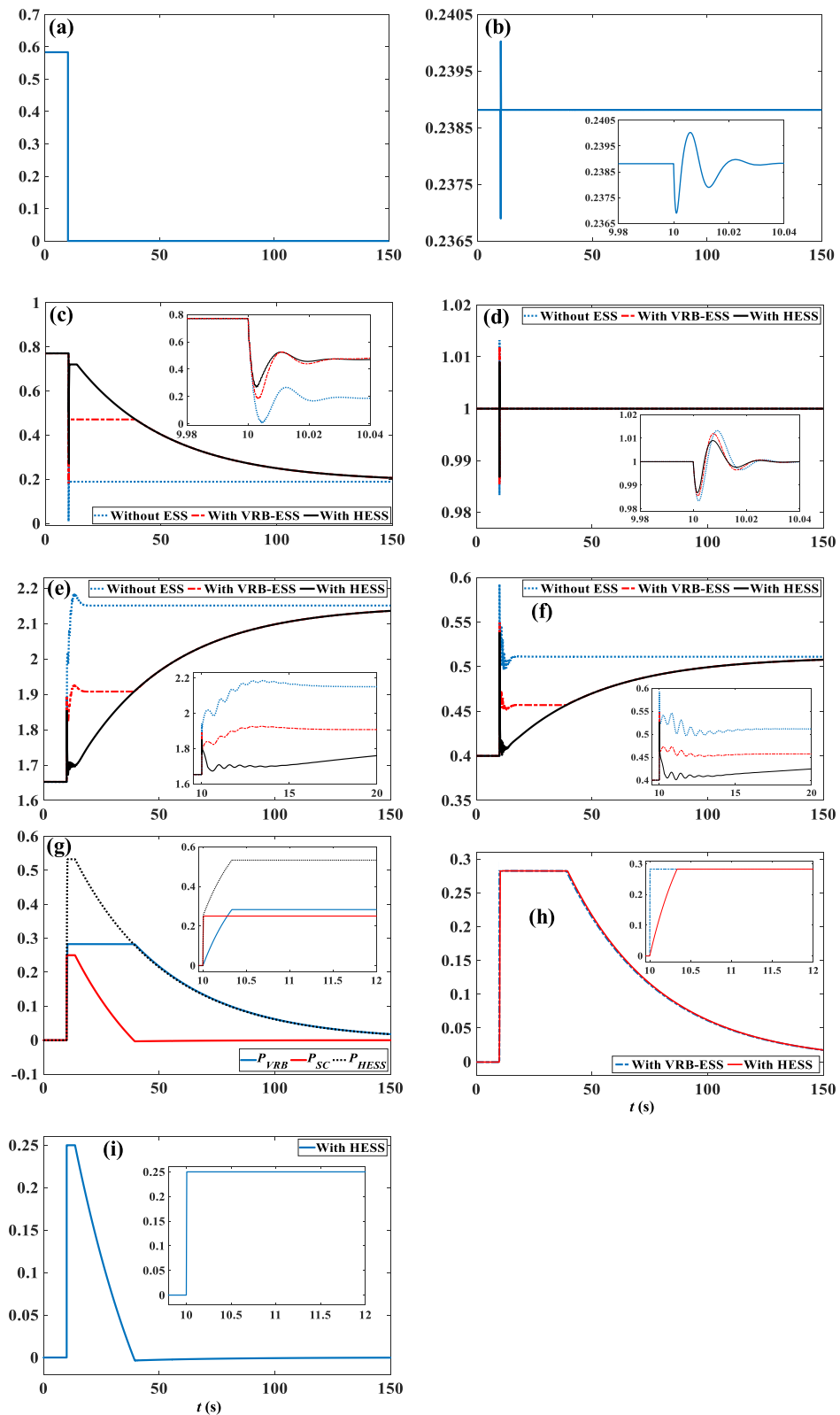


Fig. 21 Transient responses of the studied system when the studied WF is suddenly tripped at $t = 10$ s. **a** P_{PMSG} (p.u.) **b** P_{PV} (p.u.) **c** P_{BUS4} (p.u.) **d** V_{DClink} (p.u.) **e** P_{SGen1} (p.u.) **f** P_{SGen2} (p.u.) **g** P_{HESS} (p.u.) **h** P_{VRFB} (p.u.) **i** P_{SC} (p.u.)

6 Conclusions

This paper has proposed a HESS consisting of an SC and a VRFB, which has been used to stabilize the generated power from an HWPF with a WF and a PV farm fed to an MMPS. This paper has compared system-eigenvalue results for the studied system without ESS, with the VRFB-ESS, with the HESS, and has plotted the root-loci plots of the system under variable values of wind speed of the WF and the solar irradiance of the PV farm. Both dynamic and transient time-domain simulations subject to different disturbance conditions have also been performed. It can be concluded from the simulation results that the power smoothing characteristics of the studied system can be effectively improved by using the proposed HESS connected to the common DC link of the HWPF of the studied system.

Appendix

The employed parameters of the studied system are listed in Table 2.

Table 2 Employed system parameters

Single PMSG-based WTG of the studied 100-MW HWPF [19, 30]					
$P = 2 \text{ MW}, V = 690 \text{ V}, R_{PG} = 0.042, L_{dPG} = 1.05, L_{qPG} = 0.75, \psi_{PM} = 1.16$					
$H_t = 2.5 \text{ s}, H_g = 0.5 \text{ s}, K_{sh} = 0.3 \text{ (p.u.)}(\text{elec. rad})^{-1}, D_{sh} = 0.05 \text{ (p.u.)}(\text{s}(\text{elec. rad}))^{-1}$					
$c_1 = 0.5, c_2 = 116, c_3 = 0.4, c_4 = 0, c_5 = 0, c_6 = 5, c_7 = 21, c_8 = 0.08, c_9 = 0.035$					
Single PV array and DC/DC boost converter of the studied 100-MW HWPF [18, 19]					
1) PV module (SUNPOWER SPR-305E-WHT-D):					
$P_{mp} = 305.2 \text{ W}, V_{mp} = 54.7 \text{ V}, I_{mp} = 5.58 \text{ A}, N_s = 96 \text{ cells}$					
$V_{oc,n} = 64.2 \text{ V}, I_{sc,n} = 5.96 \text{ A}, R_s = 0.037998 \Omega, R_p = 993.51 \Omega$					
2) PV array: $N_{ms} = 11, N_{mp} = 150, R_{sa} = (N_{ms}/N_{mp}) \times R_s, R_{pa} = (N_{ms}/N_{mp}) \times R_p$					
3) DC/DC boost converter: $C_{pV} = 500 \mu\text{F}, R_p = 0.001 \Omega, L_p = 1.0 \text{ mH}$					
Common DC link [19, 23, 30]					
$V_{DC} = 1200 \text{ V}, C_{DC} = 0.12 \text{ F}$					
Single VRFB and the bidirectional DC/DC converter1 [31]					
1) VRFB model: $P_{VRFB} = 42 \text{ kW}, N_{cell} = 100, C_{cell} = 6 \text{ F}, R_{int} = 0.0498 \Omega$					
$R_{fix} = 11.99 \Omega, SOC_{b_Max} = 80\%, SOC_{b_Min} = 20\%$					
2) Bidirectional DC/DC converter1: $R_s = 0.01 \text{ m}\Omega, L_s = 10 \mu\text{H}$					
Single SC and the bidirectional DC/DC converter2 [19]					
1) SC model: $C_{SC} = 3000 \text{ F}, R_{sSC} = 0.29 \text{ m}\Omega, R_{pSC} = 520 \Omega$					
2) Bidirectional DC/DC converter2: $R_s = 0.01 \text{ m}\Omega, L_s = 10 \mu\text{H}$					
14-Bus Multimachine Power System [17, 32–35]					
Generator	SGen1	SGen2	SCon3	SCon4	SCon5
Rated MVA	448	100	40	25	25
Rated kV	22	13.8	13.8	13.8	13.8
Power factor (lagging)	0.85	0.85	0	0	0
X_d (p.u.)	1.67	1.18	2.373	1.25	1.25
X'_d (p.u.)	0.265	0.220	0.343	0.232	0.232
X_q (p.u.)	1.600	1.050	1.172	1.22	1.22
X'_q (p.u.)	0.460	0.380	1.172	0.715	0.715
T'_{do} (s)	0.5871	1.100	11.6	4.75	4.75
T'_{qo} (s)	0.1351	0.1086	0.159	1.5	1.5
H (s)	2.656	4.985	1.520	5.06	5.06

Acknowledgements

The authors would like to sincerely express their faithful appreciation to Buddhist Grandmaster Sheng-yen Lu for his paramount wisdom of Buddha and kind suggestions on some related research topics and papers [24–29].

Authors' contributions

Not applicable.

Funding

This research was supported in part by Higher Education Sprout Project, Ministry of Education to the Headquarters of University Advancement at National Cheng Kung University (NCKU).

Availability of data and materials

Not applicable.

Declarations

Competing interests

The authors declare no competing interests.

Received: 9 November 2022 Accepted: 26 June 2023

Published online: 14 July 2023

References

- Jing W, Hung Lai C, Wong SHW, Wong MLD. Battery-supercapacitor hybrid energy storage system in standalone DC microgrids: a review. IET Renew Power Gen. 2017;11:461–9.
- Manandhar U, Tummuru NR, Kollimalla SK, Ukil A, Beng GH, Chaudhari K. Validation of faster joint control strategy for battery- and supercapacitor-based energy storage system. IEEE T Ind Electron. 2018;65:3286–95.
- Lin PF, Wang P, Xiao JF, Wang JJ, Jin C, Tang Y. An integral droop for transient power allocation and output impedance shaping of hybrid energy storage system in dc microgrid. IEEE T Power Electr. 2018;33:6262–77.
- Xiao X, Yi H, Kang Q, Nie J. A two-level energy storage system for wind energy systems. Procedia Environ Sci. 2012;12:130–6.
- Kollimalla SK, Mishra MK, Ukil A, Gooi HB. DC grid voltage regulation using new HESS control strategy. IEEE T Sustain. Energ. 2017;8:772–81.
- Wang GS, Ciobotaru M, Agelidis VG. Power management for improved dispatch of utility-scale PV plants. IEEE T Power Syst. 2016;31:2297–306.
- Li W, Joos G, Belanger J. Real-time simulation of a wind turbine generator coupled with a battery supercapacitor energy storage system. IEEE T Ind Electron. 2010;57:1137–45.
- Wang GS, Ciobotaru M, Agelidis VG. Power smoothing of large solar PV Plant using hybrid energy storage. IEEE T Sustain Energ. 2014;5:834–42.
- Manandhar U, Ukil A, Gooi HB, Tummuru NR, Kollimalla SK, Wang BF, et al. Energy management and control for grid connected hybrid energy storage system under different operating modes. IEEE T Smart Grid. 2019;10:1626–36.
- Samosir AS, Yatim AHM. Implementation of dynamic evolution control of bidirectional DC-DC Converter for interfacing ultracapacitor energy storage to fuel-cell system. IEEE T Ind Electron. 2010;57:3468–73.
- Wee KW, Choi SS, Vilathgamuwa DM. Design of a least-cost battery-supercapacitor energy storage system for realizing dispatchable wind power. IEEE T Sustain Energ. 2013;4:786–96.
- Hajizadeh A, Golkar MA, Feliachi A. Voltage control and active power management of hybrid fuel-cell/energy-storage power conversion system under unbalanced voltage sag conditions. IEEE T Energy Convers. 2010;25:1195–208.
- Tang CH, Wang JS, Yang ZH, Jin P. Coordinated optimization control strategy for hybrid energy storage system based on real-time online analysis of power spectrum. In: 2016 2nd International Conference on Control Science and Systems Engineering (ICCSSE); Singapore; 2016.
- Hazra S, Bhattacharya S. Hybrid energy storage system comprising of battery and ultra-capacitor for smoothing of oscillating wave energy. In: 2016 IEEE Energy Conversion Congress and Exposition (ECCE). Milwaukee; 2016.

15. Pan L, Gu J, Zhu J, Qiu T. Integrated control of smoothing power fluctuations and peak shaving in wind/PV/energy storage system. In: 2016 8th International Conference on Intelligent Human-Machine Systems and Cybernetics (IHMSC). Hangzhou; 2016.
16. Wang XY, Yue M. Capacity specification for hybrid energy storage system to accommodate fast PV fluctuations. In: 2015 IEEE Power & Energy Society General Meeting. Denver; 2015.
17. Fereidouni AR, Vahidi B, Hoseini Mehr T, Tahmasbi M. Improvement of low frequency oscillation damping by allocation and design of power system stabilizers in the multi-machine power system. *Int J Elec Power*. 2013;52:207–20.
18. Wang L, Vo QS, Prokhorov AV. Dynamic stability analysis of a hybrid wave and photovoltaic power generation system integrated into a distribution power grid. *IEEE T Sustain Energ*. 2017;8:404–13.
19. Wang L, Vo QS, Prokhorov AV. Stability improvement of a multimachine power system connected with a large-scale hybrid wind-photovoltaic farm using a supercapacitor. *IEEE T Ind Appl*. 2018;54:50–60.
20. Haque ME, Negnevitsky M, Muttaqi KM. A Novel control strategy for a variable-speed wind turbine with a permanent-magnet synchronous generator. *IEEE T Ind Appl*. 2010;46:331–9.
21. Abdullah MA, Yatim AHM, Tan CW. A study of maximum power point tracking algorithms for wind energy system. In: 2011 IEEE Conference on Clean Energy and Technology (CET); Kuala Lumpur; 2011.
22. Chikh A, Chandra A. An optimal maximum power point tracking algorithm for PV systems with climatic parameters estimation. *IEEE T Sustain Energ*. 2015;6:644–52.
23. Villalva MG, Gazoli JR, Ruppert E. Comprehensive approach to modeling and simulation of photovoltaic arrays. *IEEE T Power Electr*. 2009;24:1198–208.
24. Lu SY, Wang L, Ke SC, Chang CH, Yang ZH. Evaluation of measured power quality results of a wind farm connected to Taiwan Power System. *IEEE T Ind Appl*. 2016;52:42–9.
25. Lu SY, Wang L, Lo TM, Prokhorov AV. Integration of wind power and wave power generation systems using a DC microgrid. *IEEE T Ind Appl*. 2015;51:2753–61.
26. Lu SY, Wang L. A preliminary study on total energy-density variations of a Buddhist temple in Taiwan through long-term field measurements of electric-field strength. In: 2014 IEEE Industry Application Society Annual Meeting. Vancouver; 2014.
27. Lu Sy, Wang L, Ke Sc, Chang Ch, Yang Zh. Analysis of measured power-quality results of a PV system connected to Peng-Hu power system. In: 2014 IEEE Industry Application Society Annual Meeting. Vancouver; 2014.
28. Lu SY, Wang L, Nguyen Thi H, Yang ZH, Chang Chien SY, Prokhorov AV. Impact analysis of Peng-Hu Power System connected with a photovoltaic system. In: The Green Technology and Sustainable Development (GTSD) International Conference. Hochiminh City; 2014 Oct. 30–31.
29. Lu SY, Wang L, Nguyen Thi H, Prokhorov AV. Stability enhancement of a multi-machine system using a generalized unified power-flow controller. In: The Green Technology and Sustainable Development (GTSD) International Conference. Hochiminh City; 2014 Oct. 30–31.
30. Wang L, Zeng SY, Feng WK, Prokhorov AV, Mokhlis H, Huat CK, et al. Damping of subsynchronous resonance in a hybrid system with a steam-turbine generator and an offshore wind farm using a unified power-flow controller. *IEEE T Ind Appl*. 2021;57:110–20.
31. Wang L, Huang ZH, Tseng CW, Lee MF, Tseng CC, Ku HH, et al. Operating characteristics of a vanadium redox flow battery-based energy-storage system. In: 2022 IEEE Industry Applications Society Annual Meeting (IAS). Detroit; 2022.
32. Demetriou P, Asprou M, Quiros-Tortos J, Kyriakides E. Dynamic IEEE test systems for transient analysis. *IEEE Syst J*. 2017;11:2108–17.
33. Hashim N, Hamzah N, Latip MFA, Sallehuddin AA. Transient stability analysis of the IEEE 14-Bus test system using dynamic computation for power systems (DCPS). In: 2012 Third International Conference on Intelligent Systems Modelling and Simulation. Kota Kinabalu; 2012.
34. Vittal V, McCalley JD, Anderson PM, Fouad AA. Power system control and stability. 3rd ed. Hoboken: John Wiley & Sons, Inc.; 2019.
35. Kundur PS, Malik OP. Power system stability and control. 2nd ed. New York: McGraw-Hill Education; 2022.

Publisher's Note

Springer Nature remains neutral with regard to jurisdictional claims in published maps and institutional affiliations.

Ready to submit your research? Choose BMC and benefit from:

- fast, convenient online submission
- thorough peer review by experienced researchers in your field
- rapid publication on acceptance
- support for research data, including large and complex data types
- gold Open Access which fosters wider collaboration and increased citations
- maximum visibility for your research: over 100M website views per year

At BMC, research is always in progress.

Learn more biomedcentral.com/submissions

